Available online at www.sciencedirect.com

SciVerse ScienceDirect

Acta Materialia 60 (2012) 3011–3021

Acta MATERIALIA

www.elsevier.com/locate/actamat

The relation between ductility and stacking fault energies in Mg and Mg–Y alloys

S. Sandlöbes [a,*], M. Friák [b], S. Zaefferer [a], A. Dick [b], S. Yi [c], D. Letzig [c], Z. Pei [b], L.-F. Zhu [b], J. Neugebauer [b], D. Raabe [a]

[a] *Max-Planck-Institut für Eisenforschung, Department for Microstructure Physics and Alloy Design, Max-Planck-Str. 1, 40237 Düsseldorf, Germany*
[b] *Max-Planck-Institut für Eisenforschung, Department for Computational Materials Design, Max-Planck-Str. 1, 40237 Düsseldorf, Germany*
[c] *Helmholtz-Zentrum Geesthacht, Magnesium Innovation Center, Max-Planck-Str. 1, 21502 Geesthacht, Germany*

Received 28 September 2011; received in revised form 1 February 2012; accepted 4 February 2012
Available online 7 March 2012

Abstract

The underlying mechanisms that are responsible for the improved room-temperature ductility in Mg–Y alloys compared to pure Mg are investigated by transmission electron microscopy and density functional theory. Both methods show a significant decrease in the intrinsic stacking fault I_1 energy (I_1 SFE) with the addition of Y. The influence of the SFE on the relative activation of different competing deformation mechanisms (basal, prismatic, pyramidal slip) is discussed. From this analysis we suggest a key mechanism which explains the transition from primary basal slip in hexagonal close-packed Mg to basal plus pyramidal slip in solid solution Mg–Y alloys. This mechanism is characterized by enhanced nucleation of $\langle c+a \rangle$ dislocations where the intrinsic stacking fault I_1 (ISF_1) acts as heterogeneous source for $\langle c+a \rangle$ dislocations. Possible electronic and geometric reasons for the modification of the SFE by substitutional Y atoms are identified and discussed.

Keywords: Magnesium alloys; Transmission electron microscopy (TEM); Density functional theory (DFT); Dislocation structure; Ductility

1. Introduction

Magnesium and its alloys are the lightest engineering metallic materials. They have superior potential in the fields of ultra-lightweight mobility and energy-related applications (e.g. [1,2]).

While pure Mg and most commercial wrought magnesium alloys exhibit a low room-temperature ductility (about 5% elongation for pure Mg) the addition of rare earth elements in solid solution causes a significant increase in ductility (e.g. [3–6]): Mg and single-phase solid-solution Mg–Y alloys showed an increase in room-temperature ductility by about 5 times, while maintaining comparable strength and well-balanced work hardening, through the addition of 3 wt.% Y [7]. In order to obtain deeper insight into the fundamental mechanisms responsible for this solid-solution driven ductility enhancement, density functional theory (DFT)-based methods provide a new tool to quantitatively address possible effects of Y on plasticity in these alloys [8–11]. Understanding the electronic, magnetic and geometric effects of solutes on crystalline metals at the atomic scale opens a pathway from our current phenomenological descriptive picture towards a more physics-based predictive understanding of the thermodynamic and kinetic properties of metallic materials (e.g. [8–12]). Such an approach is particularly feasible when minor alloy changes (such as in the case of solid solution Mg–Y) lead to substantial improvements in the macroscopic behaviour.

Following this approach, we present here a complementary study via joint DFT- and transmission electron microscopy (TEM)-based methods to understand the structural atomistic and electronic influence of Y on the mechanical behaviour of Mg alloys.

* Corresponding author. Tel.: +49 2116792162; fax: +49 2116792333.
E-mail address: s.sandloebes@mpie.de (S. Sandlöbes).

1359-6454/$36.00 © 2012 Acta Materialia Inc. Published by Elsevier Ltd. All rights reserved.
doi:10.1016/j.actamat.2012.02.006

In a recent study we showed that the enhancement of the mechanical properties of Mg–Y alloys is caused by a facilitated activation of additional deformation mechanisms providing a $\langle c \rangle$-deformation component, i.e. an out-of-basal-plane shear contribution [7]. Room-temperature deformation of pure Mg is limited to mainly basal $\langle a \rangle$ slip and $\{10\bar{1}2\}\langle 10\bar{1}1\rangle$ extension twinning [13,14], resulting in strain localization, shear banding and premature failure of the material [6,7]. It was observed that through alloying Y into solid solution the activity of $\{10\bar{1}1\}\langle 10\bar{1}2\rangle$ contraction [15] and $\{10\bar{1}1\}\{10\bar{1}2\}$ secondary twinning [15] as well as pyramidal $\langle c+a \rangle$ slip is much enhanced. It was suggested [16] that secondary twins promote crack nucleation. In contrast, the higher activation of $\langle c+a \rangle$ dislocations enables the material to accommodate a higher total strain through the higher number of available intrinsic deformation modes [7] and causes a more balanced work hardening. In crystal kinematic terms this means that pyramidal $\langle c+a \rangle$ slip offers five (or more) independent slip systems fulfilling the von Mises condition for general grain deformation compatibility [14], resulting in a more compatible and hence homogeneous deformation [7,8,17]. It was shown in Ref. [7] that neither grain refinement, precipitation hardening, shear banding, decreased c/a ratio nor changed Peierls potentials can be responsible for the higher activity of $\langle c+a \rangle$ dislocation slip in Mg–Y [7]. It is therefore important to investigate whether and how the addition of Y changes other materials characteristics that are critical for the ductility, such as the stacking fault energies (SFEs). A modified SFE would also affect the critical resolved shear stresses (CRSSs) associated with competing shear mechanisms, and hence would influence their relative contributions to the overall deformation.

In principle, three basal stacking faults can form in hexagonal close-packed (hcp) Mg: two intrinsic faults I_1 (stacking sequence ...ABABCBCB...) and I_2 (...ABCACAC...) and an extrinsic fault E (...ABABCABAB ...) (e.g. [8]). Previous DFT calculations of these stacking faults in pure Mg showed that the extrinsic fault (E) is energetically not favourable. For both, I_1 and I_2, relatively high SFEs (20–50 mJ m^{-2}) were obtained [8,18,19]. This results in corresponding equilibrium distance values of the partial dislocations below 1.27–1.67 nm.

2. Experimental and theoretical methods

2.1. Experimental procedure

Pure Mg, Mg–1 wt.% Y and Mg–3 wt.% Y samples were produced from 99.98% pure Mg and Y. The as-cast material was solution annealed for 20 h at 450 °C and then hot-rolled at 500 °C to a total thickness reduction of 50%. Hot rolling was performed in several passes using a laboratory rolling mill with a diameter of 200 mm, slow rolling speed of 5 rpm and a constant reduction of thickness with true strain $\varphi \leqslant 0.2$ per pass. Recrystallization annealing was performed at 500 °C for 15 min under Ar atmosphere.

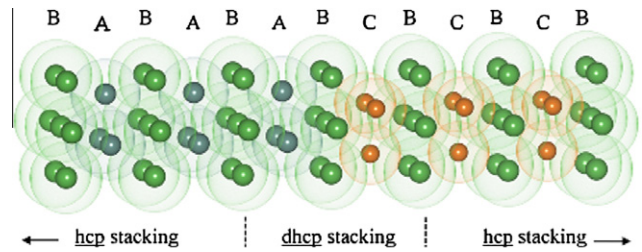

Fig. 1. Schematical drawing of the I_1 stacking fault characterized by a short double hcp (dhcp) ABCB stacking sequence separating two hcp sequences ABABAB (on the far left, green: atoms in B layers and yellow: atoms in A layers) BCBCBC (on the far right, green: atoms in B layers and orange: atoms in C layers); hcp: hexagonal close-packed structure; dhcp: double hexagonal close-packed structure. The transparent envelopes around the cores have van der Waals radii; overlapping of two envelopes indicates atomic bonding. (For interpretation of the references to color in this figure legend, the reader is referred to the web version of this article.)

Observations were performed on samples at different stages of processing. Specimens in Figs. 2–4 were 3%, respectively 5% (engineering strain), cold rolled on a laboratory mill with a roll diameter of 100 mm and a rolling speed of 20 rpm. The thickness reduction per pass was controlled to be $\varphi < 0.05$. For the analysis of the stacking fault energies (Figs. 5 and 6) fully recrystallized (15 min at 500 °C) and only slightly (<1.5% engineering strain) cold-rolled specimen were used.

For TEM observations of the dislocation reactions in Mg and Mg–Y alloys, disks 3 mm in diameter were cut by wire erosion, and then thinned to 100 μm by mechanical grinding followed by electropolishing until perforation using a twin-jet polisher (Struers TenuPol-5). The electrolyte was a solution of 3 vol.% perchloric acid in absolute ethanol. TEM observations were performed in a Philips CM20 and a FEG JEOL 2200FS at an acceleration voltage of 200 kV.

2.2. Simulation methodology

In this study, by employing DFT calculations [20,21], the intrinsic stacking fault (ISF) energies have been deter-

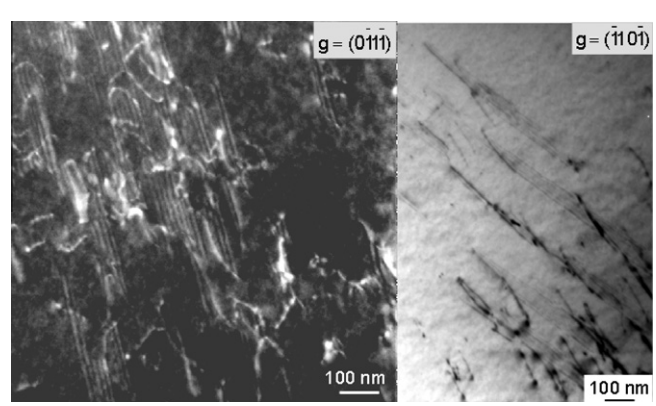

Fig. 2. TEM bright-field and dark-field images showing a high amount of stacking faults in 3% (left) and 5% (right) cold-deformed Mg–3 wt.% Y.

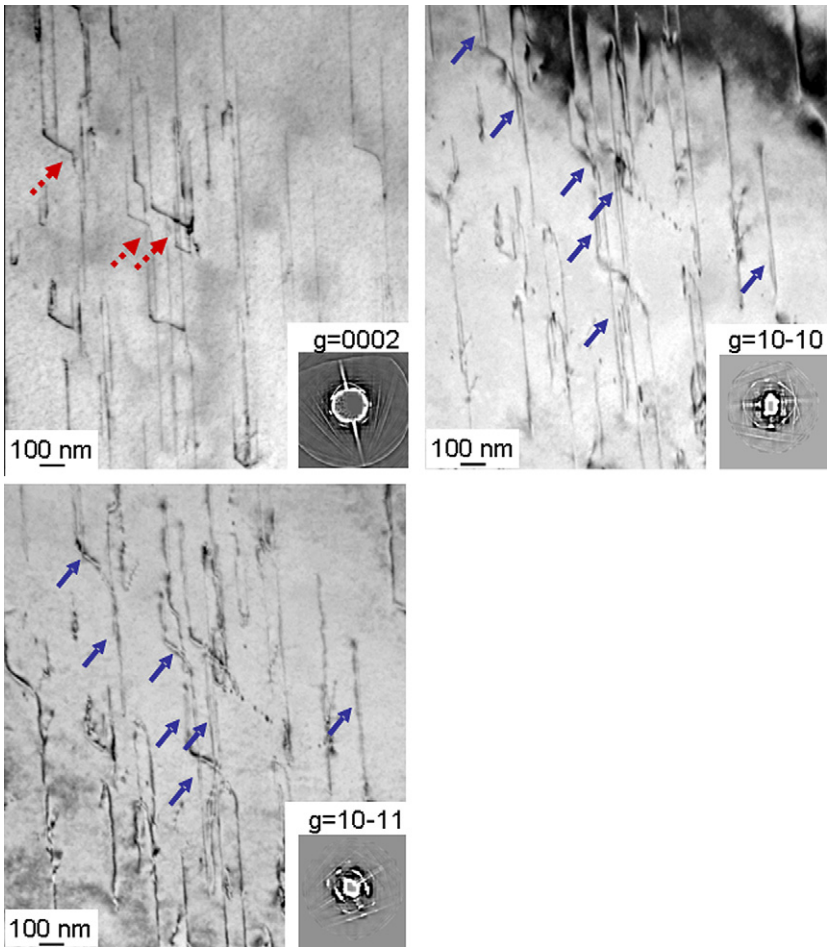

Fig. 3. TEM bright-field images under different two-beam diffractions (see inlets for the diffraction vector), showing dislocation dissociation (indicated by blue arrows) and cross-slip (indicated by red, dashed arrows) on the pyramidal plane in 3% (engineering strain) cold-rolled Mg–3 wt.% Y. (For interpretation of the references to color in this figure legend, the reader is referred to the web version of this article.)

mined within the axial next-nearest-neighbour Ising (ANNNI) framework [22]. The ANNNI model provides an accurate energetic approximation of the faulted crystal. It uses as input energies of the defect-free bulk crystals in conjunction with different stacking sequences along one of the crystallographic axes of the lattice. The approach has been successfully applied to the study of stacking faults, e.g. in austenitic stainless steels [23] and Fe–Mn alloys [24].

For analyzing compositional trends in ISF energies, the following definition of the ISF energy has been used [23]:

$$\gamma^{\mathrm{ISF}} = \frac{E^{\mathrm{ISF}} - E_0}{A}, \tag{1}$$

which is based on the energy difference between crystals with and without an ISF defect, E_{ISF} and E_0, respectively, divided by the ISF area A. Within the ANNNI model, both energies are expanded into a (theoretically infinite) series:

$$E = -\sum_n \sum_i J_n S_i S_{i+n}, \tag{2}$$

assuming that the atomic layers i and $i+n$, characterized by the corresponding spin-numbers S_i and S_{i+n}, interact via interaction parameters J_n. Truncating the series after the second term (the second-order approximation), the following expression of the first two interaction parameters is obtained:

$$J_1 = \frac{1}{2}(E_{\mathrm{hcp}} - E_{\mathrm{fcc}}), \quad J_2 = \frac{1}{2}(E_{\mathrm{dhcp}} - E_{\mathrm{fcc}} - J_1), \tag{3}$$

where the energies of the face-centred cubic (fcc) (ABCABC stacking), hcp (ABAB stacking), and double-hcp (dhcp) (ABACABAC) phases with the equilibrium volume of the hcp phase are employed. Focusing on the intrinsic stacking fault I_1 (local dhcp stacking), the energy difference between crystals with and without the stacking fault then reads:

$$E_{\mathrm{SF1}} - E_0 \approx 4J_2 - 2J_1 = 2(E_{\mathrm{dhcp}} - E_{\mathrm{hcp}}). \tag{4}$$

In this equation E_{SF1} is the I_1 SFE, E_0 is the energy of the defect-free hcp crystal, E_{hcp}, and E_{dhcp} are the total energies of hcp and dhcp, respectively. This means the I_1 SFE depends only on the energy difference between the hcp and dhcp stacking sequences of Mg–Y crystals (see Fig. 1). This procedure has the great advantage of avoiding explicit DFT simulations of the stacking faults which are numerically expensive. Instead, only the ideal hcp and dhcp

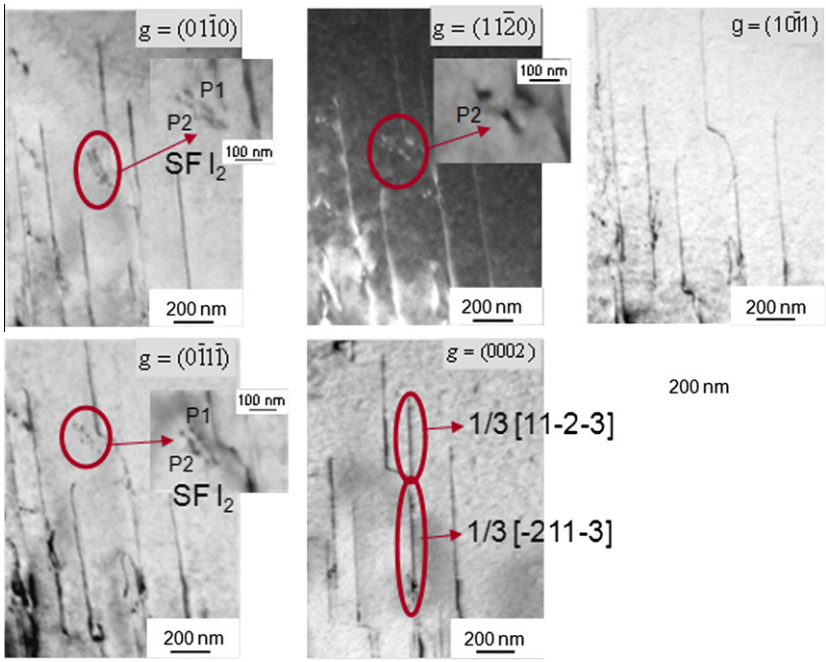

Fig. 4. TEM bright-field and dark-field images under different two-beam diffractions (see inlets for the diffraction vector), showing the activity of different perfect and partial dislocations with a $\langle c+a \rangle$ Burgers vector on pyramidal plane in 3% (engineering strain) cold-rolled Mg–3 wt.% Y; an intrinsic stacking fault I_2 (SFI_2) is also visible.

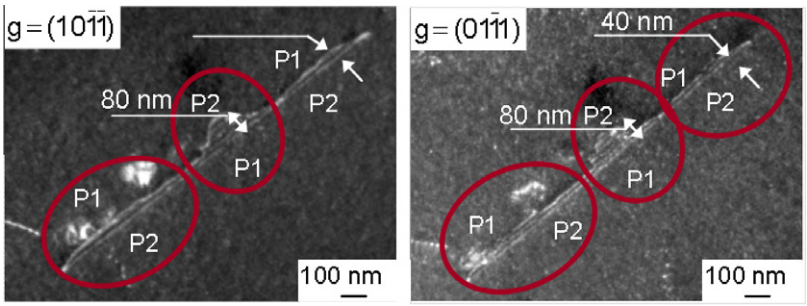

Fig. 5. TEM bright-field and weak-beam dark-field images under different two-beam diffractions (see inlets for the diffraction vector), showing I_1 stacking fault (SFI_1) in <1.5% cold-deformed Mg–3wt.% Y; P1 and P2 are the partial dislocations bounding the stacking faults. Seven more two-beam conditions were investigated to identify SFI_1.

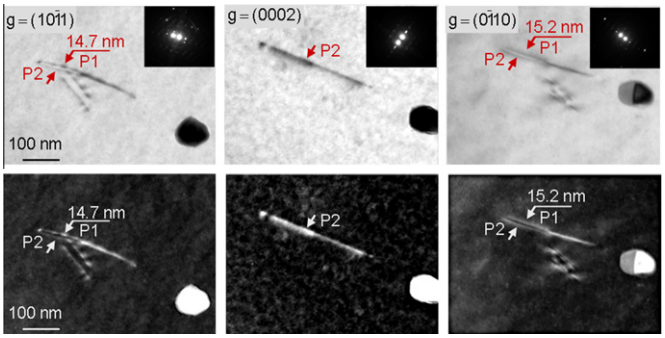

Fig. 6. TEM bright-field and weak-beam dark-field images under different two-beam diffractions (see inlets for the diffraction vector), showing I_1 stacking fault in fully recrystallized (15 min at 500 °C under Ar atmosphere) Mg–1 wt.% Y; P1 and P2 are the partial dislocations bounding the stacking faults.

bulk crystals are needed as input that are computationally inexpensive because defect-free single crystals can be represented by relatively small unit-cells (consisting of multiples of 2 or 4 atoms for hcp or dhcp, respectively) that form a single crystal by applying periodic boundary conditions.

In contrast, the explicit treatment requires calculating rather large supercells containing the full stacking fault geometry. Applying periodic boundary conditions in the explicit case gives an infinite crystal containing an array of periodically repeated stacking faults. Computational difficulties then stem from the fact that unless rather large supercells are used, the stacking fault interacts with its images. Such interactions between neighboring stacking faults do not occur in reality and thus represent an unphysical contribution to the total energy that needs to be eliminated by performing careful convergence checks with respect to the supercell size.

Table 1
Supercell geometries, number of atoms in the supercell, simulated stoichiometries, and the corresponding Monkhorst–Pack **k**-point meshes used in the DFT calculations.

	hcp	dhcp	hcp	dhcp	hcp	dhcp
at.% Y	6.25	6.25	3.125	3.125	0.926	0.926
Supercell	2 × 2 × 2	2 × 2 × 1	2 × 2 × 4	2 × 2 × 2	3 × 3 × 6	3 × 3 × 3
No. of atoms	16	16	32	32	108	108
Stoichiometry	$Mg_{15}Y_1$	$Mg_{15}Y_1$	$Mg_{31}Y_1$	$Mg_{31}Y_1$	$Mg_{107}Y_1$	$Mg_{107}Y_1$
k-point mesh	18 × 18 × 12	18 × 18 × 12	18 × 18 × 6	18 × 18 × 6	12 × 12 × 4	12 × 12 × 4

In this study the DFT calculations are performed using the Vienna Ab initio Simulation Package (VASP) [25–27]. A plane-wave basis set with an energy cut-off of 400 eV and projector augmented wave (PAW) potentials [23] have been employed. For the exchange–correlation functional the generalized gradient approximation (GGA) with the Perdew–Burke–Ernzerhof parametrization (PBE) was used [28].

The I_1 SFEs were calculated for (i) pure Mg and Y employing four-atom cells with a 36 × 36 × 12 Monkhorst–Pack **k**-point mesh, and (ii) Mg alloys containing 0.926, 3.125 and 6.25 at.% Y. The geometries of the employed supercells and the corresponding Monkhorst–Pack **k**-point meshes are summarized in Table 1.

The plane-wave basis set and the **k**-point meshes are converged to an error bar of less than 1 meV atom^{-1} when calculating SFEs. The product of the number of the Monkhorst–Pack **k**-points and the number of atoms in the supercells was kept constant and equal to 62208. Unless explicitly stated, internal coordinates of atoms within the supercells as well as the shape of the supercells were fully optimized, i.e. the total energy was minimized with respect to these degrees of freedom.

3. Results

3.1. Experimental results

TEM observations on 3% and respectively 5% (engineering strain, here and below) cold-rolled pure Mg, Mg–1 wt.% Y and Mg–3 wt.% Y alloys reveal a high density of stacking faults in the Mg–Y alloys (Fig. 2). However, in pure Mg stacking faults were observed only inside twins, known as partial stacking faults, which form during twin nucleation and growth in hcp metals [29,30].

High dislocation activities including dislocation dissociation and cross-slip on pyramidal planes were observed in 3% cold-deformed Mg–3 wt.% Y (Fig. 3). As all dislocations that appear under a diffraction vector $g = 0002$ are visible under $g = 10\bar{1}0$ as well, they are $\langle c+a \rangle$ dislocations. Burgers vector analysis of these $\langle c+a \rangle$ dislocations showed that perfect dislocations with Burgers vectors $\frac{1}{3}[11\bar{2}\bar{3}]$ and $\frac{1}{3}[\bar{2}11\bar{3}]$ as well as different partial dislocations with $b = \frac{1}{2}\langle c+a \rangle$ are formed in cold-deformed Mg–3 wt.% Y (Fig. 4).

Detailed Burgers vector (**b**) and displacement vector (**R**) analysis according to the **g**·**b** respectively **g**·**R** (**g**: diffraction vector) invisibility criteria of these stacking faults were performed and are examplary shown in Fig. 5 for Mg–3 wt.% Y and in Fig. 6 for Mg–1 wt.% Y. In order to obtain accurate data on SFEs the TEM analysis of the dislocation configurations was performed on both slightly (<1.5% strain) cold-rolled and fully recrystallized (15 min at 500 °C under Ar atmosphere) Mg–Y samples. These investigations revealed the existence of pyramidal dislocations, basal and pyramidal dislocation dipoles, and stacking faults in both alloys. The dissociation width of the stacking faults in the recrystallized samples was in the same range as those in the slightly deformed specimens (scatter of ~25% in both deformed and recrystallized specimen). For obtaining good statistics in the analysis of dislocations and stacking faults both materials (fully recrystallized and slightly deformed) are considered. This applies to both investigated alloys, Mg–1 wt.% Y and Mg–3 wt.% Y.

The analysis suggests that both types of intrinsic stacking faults occur in Mg–1 wt.% Y and Mg–3 wt.% Y. The corresponding SFEs are calculated based on the elastic equilibrium dissociation width of the partial dislocations. For this purpose we solve the Peach–Koehler equation [31,32] and consider the elastic stresses τ_{el_SF} among the partial dislocations:

$$\tau_{el\_SF} = \frac{\gamma}{b}. \tag{5}$$

The corresponding SFEs, indicated by γ in the equation, are calculated based on the experimentally observed dissociation width of the partial dislocations [33–36]:

$$\gamma = \frac{Gb^2}{8\pi d}\frac{2-\nu}{1-\nu}\left(1 - \frac{2\nu}{2-\nu}\cos 2\beta\right). \tag{6}$$

Here G is the shear modulus, ν the Poisson's ratio, b the Burgers vector of the partials, β the angle between the partials, and d the spacing of the partials. Here the values of pure Mg ($G = 16.5$ GPa, $\nu = 0.35$, $b = 1/6\ [2\bar{1}\bar{0}3]$, $1/6\ [20\bar{1}\bar{2}3]$) were also used for the solid-solution Mg–Y alloys.

In case of Mg–3 wt.% Y (Fig. 5) the experimentally observed average I_1 SFE, determined via Eq. (6) in conjunction with the experimental spacing between the partials, amounts to 1 ± 0.5 mJ m^{-2}. For I_2 (Fig. 4) the SFE of Mg–3 wt.% Y amounts to 1.5 ± 0.5 mJ m^{-2}.

As already found in Mg–3 wt.% Y, both intrinsic stacking faults are also observed in Mg–1 wt.% Y (Fig. 6). Although the dissociation width of the bounding partials associated with the I_1 stacking fault is reduced compared

Table 2
DFT-calculated I_1 SFEs γ_{SF1} (in mJ m^{-2}) in elemental Mg and Y, $Mg_{107}Y_1$, $Mg_{31}Y_1$, and $Mg_{15}Y_1$.

	Mg	$Mg_{107}Y_1$	$Mg_{31}Y_1$	$Mg_{15}Y_1$	Y
at.% Y	0	0.926	3.125	6.25	100
γ_{SF1} (mJ m^{-2})	20 ± 1	19 ± 1	14 ± 1	8 ± 1	23 ± 1

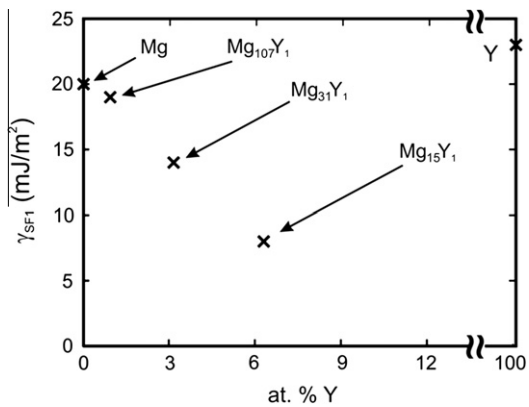

Fig. 7. The ab initio determined I_1 SFEs of Mg–Y alloys with different Y concentrations (elemental Mg and Y, $Mg_{107}Y_1$, $Mg_{31}Y_1$, and $Mg_{15}Y_1$).

to Mg–3 wt.% Y, it is still significantly lower than in pure Mg (about 85–90% lower than the SFE of pure Mg). According to Eq. (6) the I_1 SFE for Mg–1 wt.% Y amounts to 3 ± 0.7 mJ m^{-2}.

3.2. Results of the ab initio DFT simulations

The ab initio determined I_1 SFEs of Mg–Y alloys with different Y concentrations (elemental Mg and Y, $Mg_{107}Y_1$, $Mg_{31}Y_1$, and $Mg_{15}Y_1$) are summarized in Table 2 and shown in Fig. 7. Considering the whole concentration range from pure Mg to pure Y, the DFT calculations predict an unexpected non-linear compositional dependence of the I_1 SFEs γ_{SF1} in Mg–Y alloys: despite the fact that both pure elements, hcp Mg and hcp Y, have relatively high I_1 SFEs, small additions of Y into Mg result in a significant reduction of the γ_{SF1}. Specifically, the I_1 SFE of Y (23 ± 1 mJ m^{-2}) is even higher than the one of Mg (20 ± 1 mJ m^{-2}), but the I_1 SFEs, γ_{SF1}, for small additions of Y in hcp Mg ($Mg_{15}Y_1$ and $Mg_{31}Y_1$ stoichiometries) nearly linearly decrease (to 14 ± 1 mJ m^{-2} in $Mg_{31}Y_1$ and 8 ± 1 mJ m^{-2} in $Mg_{15}Y_1$) as a function of the Y concentration. The I_1 SFEs, γ_{SF1}, reduction for small Y concentrations is in qualitative agreement with the experimental data, but the absolute numbers are higher than those presented in the section above (for discussion see the following section).

4. Discussion

4.1. Introduction

Phenomenologically, the increase in ductility of solid solution Mg–Y alloys is associated with significantly increased activities of $\{10\bar{1}1\}\langle 10\bar{1}2\rangle$ contraction twinning, $\{10\bar{1}1\}\{10\bar{1}2\}$ secondary twinning, and pyramidal $\langle c+a\rangle$ dislocation slip [7]. While it has been suggested (e.g. [16]) that secondary twins promote crack nucleation, pyramidal dislocation slip is essential for the accommodation of strain along the $\langle c\rangle$-axis (e.g. [14,17]), resulting in a more compatible deformation [37–41].

The TEM experiments and first-principles calculations outlined above reveal that these higher non-basal shear activities in Mg–Y are accompanied by a significantly reduced I_1 SFE (see Sections 3.1 and 3.2 above). The trend of a reduced SFE in Mg–Y compared to pure Mg is in qualitative agreement between experiment and simulation. However, the experimental values are higher than the predicted ones. This discrepancy can be explained by, for example, (i) the difference between local and global (nominal) Y concentration, (ii) Suzuki effects (difference in Y solubility in stacking faults), and partly also (iii) intrinsic approximations within the employed computational approach. In either case we assume that the modification of the I_1 SFE is the underlying reason for the enhanced activity of pyramidal deformation mechanisms in Mg–Y alloys, i.e. allowing for the activation of sources for $\langle c+a\rangle$ dislocations. In the following sections we provide a more detailed discussion of this mechanism.

4.2. Atomic-scale mechanisms affecting shear system competition in Mg and Mg solid-solution alloys

Dislocations and dislocation-driven faults, i.e. planar faults and deformation twins, in hcp metals are geometrically rather complex. There are no simple symmetric relations between the different slip systems on basal, prism and pyramidal planes compared to, for example, fcc and bcc metals where the activated slip-systems are more symmetrically structured. With the availability of atomic-scale simulation methods several theoretical studies of dislocation core structures and dissociation behaviour in hcp metals have been performed (e.g. [8–10,11,18–20,42,47,48–51,53]). The main focus of these studies was the analysis of basal dislocation cores and reactions.

Dislocation glide velocities of basal $[11\bar{2}0]$ dislocations on basal, prism and pyramidal planes in pure Mg were calculated using molecular statics (MS) and molecular dynamics (MD) [42]. The simulations indicated the splitting of basal edge dislocations on the basal plane with a dissociation width of the partials of <2 nm in pure Mg. Other first-principles [8,18–20,43] and experimental [44–46] studies of the SFEs in pure Mg indicated relatively high basal SFEs (theoretical, via DFT and MD predictions: 20–50 mJ m^{-2}, experimental, by TEM analysis: >50 mJ m^{-2}) with a maximum equilibrium splitting of the partials of 1.27–1.67 nm in the basal plane. These calculations [8,18–20,42,43] on pure Mg are in agreement with our own current theoretical and experimental results in pure Mg, showing a relatively high SFE in pure Mg (SFE for Mg predicted by our current DFT approach: 20 ± 1 mJ m^{-2}).

Experimentally, no I_1 and I_2 stacking faults were observed in (recrystallized and slightly room-temperature deformed) pure Mg. This suggests rare dislocation dissociation and small spacings ($\leqslant$1 nm) of the partial dislocations, which is an indication for a high SFE.

A theoretical approach towards the ab initio-based prediction of the elastoplastic bulk material properties was performed in Refs. [9,48–51] by transferring elastic properties calculated from DFT into macroscopic crystal plasticity simulations for polycrystalline binary bcc Mg–Li (>30 at.% Li) and ternary Mg–Li–X alloys (where is X one of 16 different elements, e.g. Al, Si, Zn, Cu). The resulting Ashby-type strength–ductility maps revealed an inverse strength–ductility relation for the alloys studied. Importantly, different from this earlier study, our current experimental results on Mg–Y show an increase in ductility without a reduction in strength [7].

Another approach to extract DFT results and apply them to predicting mechanical properties of Mg alloys was reported in Ref. [10]. In this work DFT calculations of the respective chemical and elastic size misfit parameters of binary solid solution Mg–X alloys (where X is one of 29 solute elements) were performed. The corresponding influence of these variations in compositions on the $b = [\bar{2}110]$ basal dislocations and the I_2 SFE were discussed. These results were then used as input to the solid-solution strengthening model derived by Fleischer [52,53]. The authors concluded that the poor room-temperature ductility of Mg is caused by the restriction to mainly basal dislocation slip. The authors suggest that improving the cross-slip probability of basal dislocations onto prismatic planes in Mg would lead to an improvement in ductility. They proposed the addition of elements that cause an increase in the I_2 SFE to increase the cross-slip probability of basal dislocations.

In contrast, a decreased I_2 SFE, as found in our TEM observations, would cause (i) a lower cross-slip probability for basal dislocations and (ii) a less mobile basal dislocation structure. This might result in a relatively higher activation of non-basal deformation and, consequently, strengthening. Additionally, our current theoretical and experimental observations show a decreased I_1 SFE in conjunction with improved cross-slip on pyramidal planes, and hence improved ductility.

In Ref. [54] ab initio calculations of the elastic moduli and electronic bonding character of binary Mg–Al, Mg–Zn and Mg–Y (7.143 at.%) were performed to evaluate solid-solution strengthening in these systems. The authors used the Cauchy pressure as an indicator of the bonding character. As Mg–Y revealed the highest bond strengths in the authors' calculations, they concluded that Y might enhance the brittleness of Mg. This is opposite to our experimental results, where the addition of Y was found to cause a significant increase in ductility.

Pyramidal $\langle c+a \rangle$ dislocation slip can accommodate strain along the crystal c-axis and offers five or more independent slip systems. Therefore the nucleation of pyramidal $\langle c+a \rangle$ dislocations and their interactions are essential for explaining the ductility of hcp Mg alloys. In our current TEM experiments and in Ref. [7] we show that solid-solution addition of Y causes frequent activation of pyramidal $\langle c+a \rangle$ dislocations. As discussed in Ref. [7], grain refinement, precipitation hardening, shear banding, decreased c/a ratio and changed Peierls potentials cannot be the underlying mechanism(s) causing the observed higher activity of $\langle c+a \rangle$ dislocations in Mg–Y alloys.

The nucleation of $\langle c+a \rangle$ dislocations is the energetically critical step for plastic deformation of hcp metals and not their mobility (e.g. [17,47]). Therefore, an increase in the density of sources producing $\langle c+a \rangle$ dislocations will lead to higher pyramidal dislocation activity, resulting in an altogether higher ductility. Consequently, the addition of Y seems to promote a source mechanism for the observed $\langle c+a \rangle$ dislocations. This can be either explained in terms of Y-induced point defects, i.e. substitutional Y atoms, or Y-induced zonal defects, i.e. the observed I_1 stacking fault. As this stacking fault itself provides sessile defect structures on both, basal and pyramidal planes, we assume that it acts as the $\langle c+a \rangle$ dislocation source itself. The I_1 stacking fault is formed by removing one A plane (0001) followed by shearing along the [1 −1 0 0] direction. Consequently the local basal stacking sequence changes from ABABAB to ABABCBCB. I_1 is a sessile defect and cannot itself contribute to or be created via plastic deformation. Rather, it must be formed by condensation of vacancies on basal planes. Although the I_1 stacking fault is known as a basal stacking fault as it changes the basal stacking sequence, it is not of purely basal character (see e.g. Fig. 1). The I_1 stacking fault is bound by Frank-type pyramidal ½ $\langle c+a \rangle$ partial dislocations (1/6 [11−23], e.g. 1/6 [2−203], 1/6 [20−23], or respectively 1/6 [02−23]) (e.g. [14,55,56]), i.e. the I_1 stacking fault forms defect structures on pyramidal planes.

In the light of the DFT predicted and experimentally observed reduced SFEs we assume that the sessile I_1 stacking fault acts as the heterogeneous source for the observed $\langle c+a \rangle$ dislocations. Due to the complex structure and non-Schmid behavior (with respect to the expected Schmid-factors) of pyramidal dislocations (cores) in hcp metals, only little is known about their nucleation. Yoo et al. [17,47] proposed a nucleation model for $\langle c+a \rangle$ dislocations in hcp metals in which the interaction of (mobile) $\langle a \rangle$ and a (sessile) $\langle c \rangle$ dislocation creates sessile nodes. These nodes are assumed to pin $\langle c+a \rangle$ dislocations, which in turn may continuously emit further $\langle c+a \rangle$ dislocations. The I_1 stacking fault that we observed experimentally in this work may act in a similar fashion as the sessile nodes described in Refs. [17,47]: (i) it first forms a sessile pyramidal defect (partial dislocation) and (ii) then acts as an obstacle for other dislocations, i.e. it can pin $\langle a \rangle$ and $\langle c \rangle$ dislocations.

Experimentally we observed the I_1 stacking fault in the non-deformed state, indicating a thermal activation. This is in accordance with our DFT calculations showing locally

equal energies for the hcp (Mg) and dhcp (SFI_1) stacking sequences. After slight plastic deformation (3% engineering strain) we observed high activity of pyramidal dislocations in the Mg–1 wt.% Y and Mg–3 wt.% Y alloys. Besides split pyramidal dislocations, perfect pyramidal dislocations and their cross-slip on pyramidal planes were observed (Fig. 3). This supports our assumption that (i) the nucleation of $\langle c+a \rangle$ dislocations is causing the enhanced ductility, and (ii) the observed I_1 stacking fault acts as source for these $\langle c+a \rangle$ dislocations. Cross-slip is a main carrier of ductility in hcp metals as it allows dynamic recovery during deformation. Thus, we conclude that the main difference between the brittle pure Mg and the ductile Mg–Y is the more easy nucleation of $\langle c+a \rangle$ dislocations in Y alloyed Mg.

Understanding why Y causes the observed reduction of the I_1 SFE in Mg is only possible using quantum mechanical calculations. In the following sections we provide a detailed analysis of the geometric and electronic effects of Y on the I_1 SFE using DFT.

4.3. Individual energy contributions affecting stacking fault energy modification

Pyramidal dislocation cores as well as dislocation reactions involving non-basal planes are non-planar involving several planes with rather complex atomic configurations (e.g. [8,11]). This inherent structural complexity renders their exact DFT analysis computationally demanding. Therefore, we employ the second-order ANNNI model that approximates the I_1 SFE to be proportional to the total energy difference between the dhcp (stacking of the SFI_1) and hcp (defect-free Mg stacking) stacking sequences at the equilibrium volume of the hcp phase as outlined above (see Eq. (4)).

The detailed analysis of these two stacking sequences and their dependence on alloy composition is of importance in this context as they determine the I_1 SFE value that finally matters for the activation of non-basal slip contributions. Furthermore, analyzing the ab initio data can uniquely provide a comprehensive insight into the fundamental mechanisms (i.e. volumetric aspects of solid solution or electronic-structure properties) behind the reduction of the I_1 SFE as a function of the Y content. Identification of these volumetric and electronic effects of Y on the SFEs in Mg might provide criteria for the selection of further alloying elements with similar effect on the mechanical properties, particularly on ductility.

For this purpose, the total energy differences between the hcp (defect-free Mg) and dhcp (SFI_1 stacking) stacking sequences is decomposed into their strain-free and elastic-strain-dependent contributions (see Fig. 8). These portions are then individually investigated. In Table 3 the calculated thermodynamic, structural and elastic properties of pure Mg, pure Y and Mg–Y alloys are summarized.

The calculated ($E_{dhcp} - E^{eq}_{hcp}$) energy differences (see the second row of Table 3, Fig. 9a) consist of two parts. The

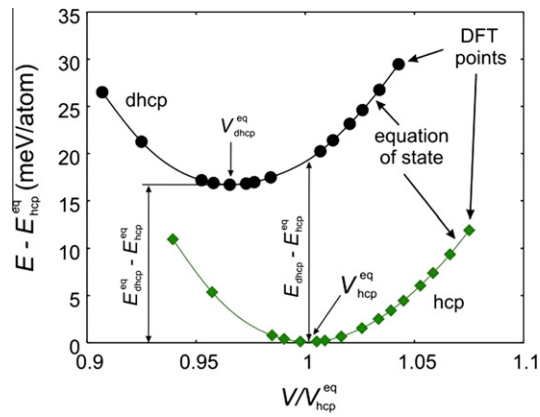

Fig. 8. Schematic figure of the energy–volume curves calculated for both hcp and dhcp phases. The solid lines are fitted to the ab initio results using Murnaghan's equation of state [57]. The schematic sketch also illustrates the meaning of the various energy/volume-related parameters used in the ANNNI model.

first part is the strain-free total energy difference ($E^{eq}_{dhcp} - E^{eq}_{hcp}$) between both stacking types (hcp and dhcp) at their respective equilibrium volumes (see the third row in Table 3 for values and Fig. 8 for an explanation of the used terminology). Here E_{dhcp} is the energy of the dhcp stacking, E^{eq}_{hcp} is the energy of the hcp stacking sequence at its equilibrium volume, and E^{eq}_{dhcp} is the energy of the dhcp stacking at its equilibrium volume (see schematic Fig. 8 for explanation). The second part is the strain energy contribution to the total energy of the dhcp stacking, i.e. the I_1 stacking fault. The strain energy contribution arises due to the fact that the dhcp-like stacking fault I_1 locally adopts the equilibrium in-plane geometry of the hcp defect-free matrix that is surrounding it.

Since the results for the c/a ratio for hcp and dhcp stacking sequences are essentially identical for all calculated Mg–Y alloys, except for elemental Y (see Table 3 and Fig. 9b), the out-of-plane relaxations should not influence the interlayer distance within the ISF. This means that if the dhcp phase adopts the equilibrium volume and lattice parameters of the hcp matrix (c/a ratio hcp = ½ c/a dhcp), the lattice strain induced in the matrix by the stacking fault is minimized. As this strain contributes to the formation energy of the stacking fault, i.e. the SFE, the SFE is reduced as well.

The strain-free (electronic) energy difference between hcp and dhcp stackings decreases with increasing Y content from 5.7 meV atom^{-1} in elemental hcp Mg to 3.9 meV atom^{-1} in $Mg_{31}Y_1$ and 2.4 meV atom^{-1} in $Mg_{15}Y_1$. This is rather unexpected considering the fact that the strain-free energy difference between hcp and dhcp stacking is in pure hcp Y even higher (8.4 meV atom^{-1}) than that predicted in pure hcp Mg. The computed reduction of the strain-free energy difference is likely caused by complex interactions between Mg and Y that also result in a non-trivial Mg–Y phase diagram exhibiting a number of structurally complex stoichiometric compounds.

Table 3
DFT-calculated parameters of the hcp and dhcp phases: total energy (E) differences between the hcp and dhcp states with the volume equal to the equilibrium volume of the hcp phase, the equilibrium atomic volumes V (in Å^3 atom^{-1}), the bulk moduli B (in GPa) together with the lattice parameter (c/a) ratio of elemental Mg and Y, $Mg_{107}Y_1$, $Mg_{31}Y_1$, and $Mg_{15}Y_1$. The energy difference in brackets for Y indicates the value without the volumetric-energy contribution, i.e. the energy difference is calculated from the energies of the hcp and dhcp states with their corresponding equilibrium volume.

	Mg	$Mg_{107}Y_1$	$Mg_{31}Y_1$	$Mg_{15}Y_1$	Y
at.% Y	0	0.926	3.125	6.25	100
$E_{dhcp} - E^{eq}_{hcp}$ (meV atom^{-1})	5.7	5.1	3.9	2.4	8.5 (7.8)
V_{dhcp} (Å^3 atom^{-1})	23.030	23.126	23.341	23.695	32.463
V_{hcp} (Å^3 atom^{-1})	22.956	23.058	23.318	23.706	32.880
$(V_{dhcp} - V_{hcp})/V_{hcp}$	0.32%	0.30%	0.10%	−0.05%	−1.27%
B_{dhcp} (GPa)	35.0	35.5	35.9	35.8	39.3
B_{hcp} (GPa)	35.4	35.9	36.2	35.9	40.2
$(B_{dhcp} - B_{hcp})/B_{hcp}$	−0.99%	−1.14%	−0.82%	−0.38%	−2.49%
$(c/a)_{hcp}$	1.628	1.625	1.609	1.582	1.549
½$(c/a)_{dhcp}$	1.636	1.632	1.612	1.587	1.608

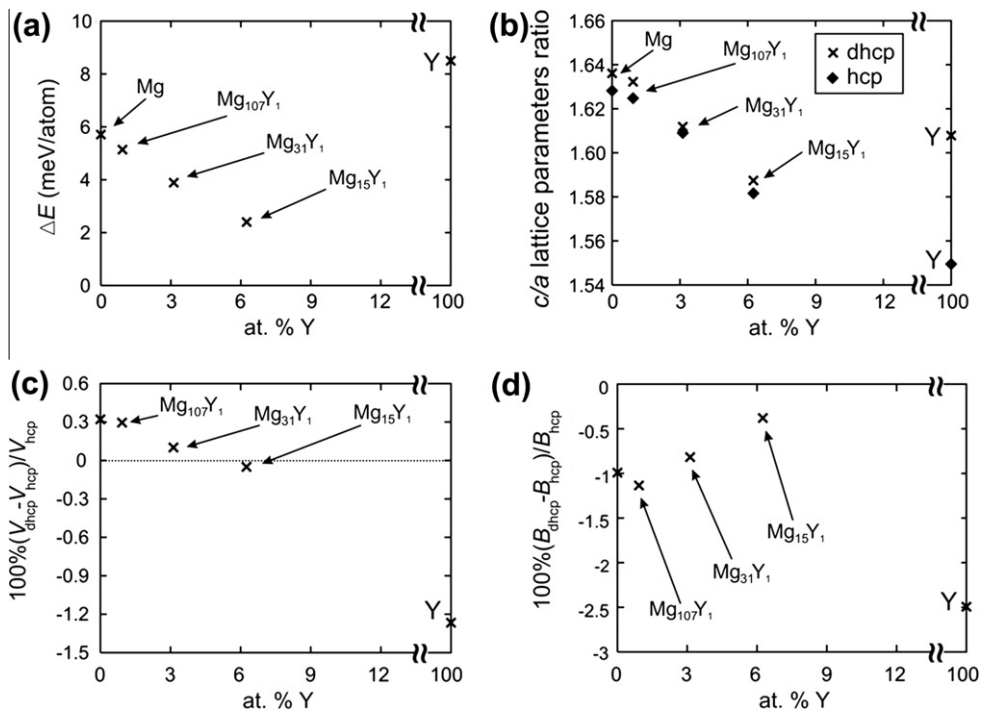

Fig. 9. Computed compositional trends of energy differences (a), the hcp and dhcp lattice parameter c/a ratios (b), and relative differences (in %) of volumes V (c) and bulk moduli B (d) between the hcp and dhcp phases (hcp: hexagonal close-packed structure; dhcp: double hexagonal close-packed structure).

The volumetric-strain part of the energy is very small in all compounds studied (within the computational error, i.e. up to 0.1 meV atom^{-1}), except for elemental Y (see the strain-free energy difference in Y in Table 3 in brackets). The non-negligible volumetric-strain energy in Y mostly stems from a higher difference between the hcp and dhcp equilibrium volumes (−1.27%). The value exceeds the difference predicted for the other compounds under investigation (Mg, Mg–Y). Since the overall trend in the strain-free energy difference is similar to that predicted for the I_1 SFEs (Table 2), it can be concluded that the reduction of the strain-free energy difference between the hcp and dhcp stackings represents a main contribution to the I_1 SFE reduction in Mg–Y alloys. Due to the fact that the strain-free energy difference between the hcp and dhcp stackings is also a measure of stability of the hcp stacking with respect to the dhcp one, any reduction of this difference also indicates a lower stability of the hcp stacking.

4.3.1. Strain-energy effect on the ISF_1 in Mg–Y

To better understand the reasons that cause the reduced I_1 SFE, further analysis of different contributions to this strain-free energy difference was performed. Specifically, the volumetric difference between the equilibrium volumes of both stacking sequences (hcp and dhcp) and the volumetric compressibility of the dhcp stacking sequence, represented by its bulk modulus, are analyzed. Based on these two quantities, the volumetric-strain energy part of

the total energy differences of the hcp and dhcp stackings is evaluated using the Murnaghan equation of state [57].

As far as the lattice parameters are concerned, the c/a ratio decreases in both calculated bulk structures, hcp and dhcp, when replacing Mg by Y. The $(c/a)_{hcp}$ respectively $\frac{1}{2}(c/a)_{dhcp}$ ratios are listed in Table 3 and shown in Fig. 9b. This comparison is pertinent as the dhcp unit cell is defined by twice as many atomic planes (the ABAC sequence is being repeated) compared to the hcp structure (only the AB sequence is being repeated). Here it seems that the compositional trend in the $(c/a)_{hcp}$ ratio is nearly identical to that predicted for the $\frac{1}{2}(c/a)_{dhcp}$ ratio, again, with the pure solute, the elemental Y, being the only exception.

As seen in Table 3, the equilibrium atomic volume increases with increasing Y concentration in agreement with the fact that the equilibrium volume of hcp Y is significantly higher compared to that of hcp Mg ($V_{eq}^{Y}/V_{eq}^{Mg} = 1.432$, where V_{eq}^{Y} is the equilibrium volume of Y and V_{eq}^{Mg} is the equilibrium volume of Mg). Despite the fact that these compositional trends are qualitatively similar for both, hcp and dhcp stackings, the actual trends are not equal. There are differences in the equilibrium atomic volumes of the respective hcp and dhcp stacking structures (see Fig. 9c). The equilibrium volume of the dhcp Mg is 0.32% higher than that of ground-state hcp Mg in contrast to Y in which the volume of the dhcp phase is smaller by 1.27% than that of hcp Y. For $Mg_{15}Y$ the hcp and dhcp volumes are predicted to be nearly identical, i.e. at the local concentration $Mg_{15}Y$ the predicted ISF_1 SFE is minimized (Fig. 9c).

DFT predicted bulk moduli (see Table 3 and Fig. 9d) are quite similar for the hcp and dhcp stacking sequences in the studied compositions (except for Y) and the dhcp stacking sequences are predicted to be elastically softer than the corresponding hcp ones. The difference of the bulk moduli between the hcp and dhcp stacking sequences is −0.99% in Mg and −2.49% in Y, but it is significantly reduced (to −0.38%) in $Mg_{15}Y$ (see Fig. 9d). Similar as for the stacking fault energies and structural parameters discussed above, differences in the elasticity of hcp and dhcp stackings are lower in Mg–Y alloys than in pure Mg. Thus, the addition of Y makes both types of stacking (defect-free hcp and stacking-fault-like dhcp) energetically, structurally and elastically nearly identical. Here we suppose that by this the thermodynamic driving force needed to form the stacking faults is significantly reduced. From a materials-design point of view this similarity of both stackings is a strong indication for the selection of alternative alloying elements to improve the ductility of Mg alloys.

5. Conclusions

The ductility increase through the addition of Y to Mg is related to higher activities of $\langle c+a \rangle$ dislocation slip providing an additional $\langle c \rangle$-deformation component in Mg–Y alloys. This facilitated activation of out-of-basal-plane shear modes is accompanied by a significantly decreased I_1 SFE through the addition of Y. We propose that this modification of the I_1 SFE is the main reason behind the ductility increase in the Mg–Y system acting as follows:

(i) The enhanced ductility is caused by a high activity of pyramidal $\langle c+a \rangle$ dislocations as slip modes out of the basal plane are a main mechanism for the ductilization of Mg alloys owing to the von Mises criterion for compatible deformation.
(ii) The nucleation of $\langle c+a \rangle$ dislocations is the critical step in providing out-of-basal-plane shear. It is associated with the I_1 stacking fault. The sessile I_1 stacking fault, whose energy decreases with Y alloying, is bound by pyramidal partial dislocations. This structural effect enables the formation of dislocation structures on pyramidal planes. According to the nucleation model of Yoo et al. [17,47] we suggest that the I_1 stacking fault acts as heterogeneous nucleation source for pyramidal $\langle c+a \rangle$ dislocations.
(iii) The observed (TEM) and calculated (DFT) reduced I_1 SFE through the addition of Y, causing the formation of stable SFI_1 in Mg–Y alloys, and hence sources for $\langle c+a \rangle$ dislocations.

To further analyze the underlying mechanisms of the experimentally observed reduction of the I_1 stacking fault ab initio calculations are performed. From these ab initio calculations we conclude that the reduced I_1 SFE is a direct consequence of two different phenomena. First, the thermodynamic (strain-free) stability of hcp stacking sequences (defect-free Mg–Y solid solution) is significantly reduced with respect to dhcp stacking sequences (SFI_1) when the Y concentration approaches locally its solubility limit in Mg. Second, lowering of the SFE is accompanied by significant reduction of structural and elastic differences between hcp and dhcp stacking sequences. Here the defect-free stacking sequence is hcp, while the I_1 stacking fault causes local dhcp stacking. Both hcp and dhcp phases are predicted to be structurally very similar, matching both in terms of lattice parameters and corresponding c/a ratios. This means that the strain-energy part of the I_1 SFE is minimized. The combination of these two phenomena is the underlying mechanism for the theoretically and experimentally observed reduction in the I_1 SFE.

Acknowledgments

The authors are grateful to the Deutsche Forschungsgemeinschaft (DFG) for financial support through the project "Fundamental investigation of the mechanisms of deformation and recrystallisation of cold deformable Mg alloys micro-alloyed with rare earth elements and microstructure optimization for the development of a new class of Mg-alloys", Grant YI 103 1-2/ZA 278 6-2.

References

[1] Agnew SR, Nie JF. Scripta Mater 2010;63:671–3.
[2] Kainer KU, Yuanding H, Dieringa H, Hort N. Mater Sci Forum 2010;638–642:73–80.
[3] Couling SL, Pashak JF, Sturkey L. Trans ASM 1959;51:94–107.
[4] Chino Y, Kado M, Mabuchi M. Acta Mater 2008;56:387–94.
[5] Chino Y, Kado M, Mabuchi M. Mater Sci Eng A 2008;494(1–2): 343–9.
[6] Barnett MR, Nave MD, Bettles CJ. Mater Sci Eng A 2004;386(1–2): 205–11.
[7] Sandlöbes S, Zaefferer S, Schestakow I, Yi S, Gonzales-Martinez R. Acta Mater 2011;59(2):429–39.
[8] Yasi JA, Nogaret T, Trinkle DR, Qi Y, Hector Jr LG, Curtin WA. Model Simul Mater Sci Eng 2009;17:055012 [13pp].
[9] Counts WA, Friák M, Raabe D, Neugebauer J. Acta Mater 2009;57:69–76.
[10] Yasi JA, Hector Jr LG, Trinkle DR. Acta Mater 2010;58:5704–13.
[11] Nogaret T, Curtin WA, Yasi JA, Hector Jr LG, Trinkle DR. Acta Mater 2010;58:4332–43.
[12] Raabe D, Sander B, Friák M, Ma D, Neugebauer J. Acta Mater 2007;55:4475–87.
[13] Barnett MR. Mater Sci Eng A 2007;464:1–7.
[14] Yoo MH. Metall Trans A Phys Metall Mater Sci 1981;12:409–18.
[15] Barnett MR. Mater Sci Eng A 2007;464:8–16.
[16] Koike J, Fujiyama N, Ando D, Sutou Y. Scripta Mater 2010;63:747–50.
[17] Yoo MH, Morris JR, Ho KM, Agnew SR. Metall Mater Trans A 2002;33:813–22.
[18] Smith AE. Surf Sci 2007;601:5762–5.
[19] Wen L, Chen P, Tong Z-F, Tang B-Y, Peng L-M, Ding W-J. Eur Phys J B 2009;72:397–403.
[20] Hohenberg P, Kohn W. Phys Rev B 1964;136(3B):B864–71.
[21] Kohn W, Sham LJ. Phys Rev A 1965;140(4A):A1133–8.
[22] Denteneer PJH, van Haeringen W. J Phys C: Solid State Phys 1987;20(32):L883–7.
[23] Vitos L, Nilsson J-O, Johansson B. Acta Mater 2006;54:3821–6.
[24] Dick A, Hickel T, Neugebauer J. Steel Res Int 2009;80(9):603–8.
[25] Kresse G, Hafner J. Phys Rev B 1993;47(1):558–61.
[26] Kresse G, Furthmuller J. Phys Rev B 1996;54(16):11169–86.
[27] Blöchl PE. Phys Rev B 1994;50(24):17953–79.
[28] Perdew JP, Burke K, Ernzerhof M. Phys Rev Lett 1996;77(18): 3865–8.
[29] Song SG, Gray III GT. Philos Mag A 1995;71(2):263–74.
[30] Tomsett DI, Bevis M. Philos Mag A 1969;19(159):533–7.
[31] Koehler JS. Phys Rev 1941;60:397–410.
[32] Peach M, Koehler JS. Phys Rev 1950;80(3):436–9.
[33] Hirth P, Lothe J. Theory of dislocations. 2nd ed. New York: John Wiley & Sons; 1982.
[34] Stevens R, Miles LJ. J Mater Sci 1976;11:1911–8.
[35] Christian JW, Vitek V. Rep Prog Phys 1970;33:307–411.
[36] Buff Jr AW. Metall Trans 1970;1:2391–413.
[37] Chino Y, Sassa K, Mabuchi M. Mater Sci Eng A 2009;513–514:394–400.
[38] Yi S, Bohlen J, Heinemann F, Letzig D. Acta Mater 2010;58(2): 592–605.
[39] Dreyer CE, Chiu WV, Wagoner RH, Agnew SR. J Mater Process Technol 2010;210:37–47.
[40] Gehrmann R, Frommert MM, Gottstein G. Magnesium. In: Kainer KU, editor. Proc magnesium alloys and their applications. Weinheim: Wiley-VCH Verlag; 2010. p. 142–8.
[41] Jianxin Z, Sinclair C, Wagner F. Magnesium. In: Kainer KU, editor. Proc magnesium alloys and their applications. Weinheim: Wiley-VCH Verlag; 2010. p. 238–44.
[42] Groh S, Marin EB, Horstemeyer MF, Bammann DJ. Model Simul Mater Sci Eng 2009;17:075009 [15pp].
[43] Wu X, Wang R, Wang S. Appl Surf Sci 2010;256:3409–12.
[44] Harris JE, Masters BC. Proc Roy Soc (Lond) 1966;A292:240–4.
[45] Hales R, Smallman RE, Dobson PS. Proc Roy Soc (Lond) 1968;A307:71–81.
[46] Sastry DK, Prasad YVRK, Vasu KI. Scripta Met 1969;3:927–30.
[47] Yoo MH, Agnew SR, Morris JR, Ho KM. Mater Sci Eng A 2001;310–321:87–92.
[48] Counts WA, Friák M, Battaile CC, Raabe D, Neugebauer J. Phys Status Solidi B 2008;245(12):2630–5.
[49] Counts WA, Friák M, Raabe D, Neugebauer J. Adv Eng Mater 2010;12(7):572–6.
[50] Counts WA, Friák M, Raabe D, Neugebauer J. Adv Eng Mater 2010;12:1198–205.
[51] Counts WA, Friák M, Raabe D, Neugebauer J. Magnesium. In: Kainer KU, editor. Proc magnesium alloys and their applications. Weinheim: Wiley-VCH Verlag; 2009. p. 133–7.
[52] Fleischer RL, Peckner D, editor. The strength of metals; 1964. p. 93–140.
[53] Fleischer RL. J Appl Phys 1962;33(12):3504–8.
[54] Chen K, Boyle KP. Metall Mater Trans A 2009;40(11):2751–60.
[55] Zhu YM, Morton AJ, Weyland M, Nie JF. Acta Mater 2010;58:464–75.
[56] Ando S, Gotoh T, Tonda H. Metall Mater Trans A 2002;33(3):823–9.
[57] Murnaghan FD. Proc Natl Acad Sci USA 1944;30:244.